Magnetic Resonance Imaging 33 (2015) 374–384

Contents lists available at ScienceDirect

Magnetic Resonance Imaging

journal homepage: www.mrijournal.com

Incorporating relaxivities to more accurately reconstruct MR images

Muge Karaman [a], Iain P. Bruce [b], Daniel B. Rowe [c,d,*]

[a] Center for MR Research, University of Illinois at Chicago, Chicago, IL, USA
[b] Duke/UNC Brain Imaging and Analysis Center, Duke University, Durham, NC, USA
[c] Department of Mathematics, Statistics, and Computer Science, Marquette University, Milwaukee, WI, USA
[d] Department of Biophysics, Medical College of Wisconsin, Milwaukee, WI, USA

ARTICLE INFO

Article history:
Received 29 August 2014
Revised 8 January 2015
Accepted 9 January 2015

Keywords:
Magnetic resonance imaging (MRI)
Functional MRI (fMRI)
MR relaxivities
Longitudinal relaxation time (T_1)
Image reconstruction
Correction

ABSTRACT

Purpose: To develop a mathematical model that incorporates the magnetic resonance relaxivities into the image reconstruction process in a single step.
Materials and methods: In magnetic resonance imaging, the complex-valued measurements of the acquired signal at each point in frequency space are expressed as a Fourier transformation of the proton spin density weighted by Fourier encoding anomalies: T_2^*, T_1, and a phase determined by magnetic field inhomogeneity (ΔB) according to the MR signal equation. Such anomalies alter the expected symmetry and the signal strength of the *k*-space observations, resulting in images distorted by image warping, blurring, and loss in image intensity. Although T_1 on tissue relaxation time provides valuable quantitative information on tissue characteristics, the T_1 recovery term is typically neglected by assuming a long repetition time. In this study, the linear framework presented in the work of Rowe et al., 2007, and of Nencka et al., 2009 is extended to develop a Fourier reconstruction operation in terms of a real-valued isomorphism that incorporates the effects of T_2^*, ΔB, and T_1. This framework provides a way to precisely quantify the statistical properties of the corrected image-space data by offering a linear relationship between the observed frequency space measurements and reconstructed corrected image-space measurements. The model is illustrated both on theoretical data generated by considering T_2^*, T_1, and/or ΔB effects, and on experimentally acquired fMRI data by focusing on the incorporation of T_1. A comparison is also made between the activation statistics computed from the reconstructed data with and without the incorporation of T_1 effects.
Result: Accounting for T_1 effects in image reconstruction is shown to recover image contrast that exists prior to T_1 equilibrium. The incorporation of T_1 is also shown to induce negligible correlation in reconstructed images and preserve functional activations.
Conclusion: With the use of the proposed method, the effects of T_2^* and ΔB can be corrected, and T_1 can be incorporated into the time series image-space data during image reconstruction in a single step. Incorporation of T_1 provides improved tissue segmentation over the course of time series and therefore can improve the precision of motion correction and image registration.

1. Introduction

In magnetic resonance imaging (MRI), data are acquired in the spatial frequency domain and reconstructed through an inverse Fourier transform, into images of the object in the image domain. Thus, the measured *k*-space data, encoded in time, are generally expected to be the Fourier transform of the proton spin density. However, in the process of Fourier encoding in echo planar imaging (EPI), the detected MRI signal is subject to the MR relaxivities, T_2^* and T_1, as well as magnetic field inhomogeneity, ΔB, commonly referred to as Fourier anomaly. The physical mechanisms behind the Fourier encoding process cause image artifacts or image distortions. One such effect is the one caused by acquiring measurements of *k*-space at different times after the RF excitation pulse. Due to the non-instantaneous acquisition of each *k*-space line, the first points sampled have a lower T_2^* weighting than the subsequent points. Considering that the "ideal" image would be reconstructed from the "ideal" *k*-space measurements, in which every point is sampled with the exact same weighting, the "actual" acquired *k*-space measurements in practice are scaled according to the time by a factor determined by T_2^* [1,2]. As such, the "actual" reconstructed image, which is obtained by an inverse Fourier transformation of the "actual" *k*-space measurements, has a blurring effect in the phase encoding direction as a result of the inverse Fourier transformation of this weighting pattern. Moreover, the differences in magnetic susceptibility

* Corresponding author at: Department of Mathematics, Statistics, and Computer Science, Marquette University, Milwaukee, Wisconsin, USA. Tel.: +1 414 288 5228; fax: +1 414 288 5472.
E-mail address: daniel.rowe@marquette.edu (D.B. Rowe).

http://dx.doi.org/10.1016/j.mri.2015.01.003
0730-725X/

between tissues or magnetic materials lead to incorrect sampling of k-space by introducing errors in the gradients. Thus, the point in k-space that is believed to be sampled is not the actual location. As such, magnetic field inhomogeneities incur spatial distortions including image warping and phase generation. Although the weighting through T_1 is not affected by the non-instantaneous sampling of k-space, it can modulate the MR signal resulting in signal loss and image weighting that depend on the tissue characteristics. The artifacts resulting from $T_2{}^*$ relaxation during sampling, the inhomogeneities in the magnetic field, and the alteration in the signal arising from the longitudinal relaxation can be considered as $T_2{}^*$, ΔB, and T_1 effects, respectively,

Correcting the image warping effects of both the static and dynamic magnetic field inhomogeneities [3–7], and reducing the T_2^* blurring effect [8–11] in EPI sequences have been active areas of research in brain imaging. Despite such efforts for correcting T_2^* and ΔB effects, conventional studies do not account for a recovery of the longitudinal relaxation time; instead they use the standard assumption of a long repetition time. However, this assumption is not always valid, and the signal amplitude becomes dependent on T_1 when performing fast repetitive image excitations with incomplete recovery of the longitudinal magnetization. Moreover, T_1 relaxation time provides a robust contrast mechanism for distinguishing tissue type [12]. This quantitative knowledge of tissue characteristics, which can be extracted from the data acquired during the transient state prior to T_1 equilibrium, can be incorporated into the reconstructed image-space time series data. It has been suggested in previous studies that the image registration performance can be improved with increased tissue contrast [13–16]. Therefore, T_1 incorporated time series images, which would have appreciably higher tissue contrast, can potentially lead to improved image registration.

As noted before, the Fourier anomalies appear as exponential terms in the traditional signal equation, and therefore the observed k-space measurements can be considered as the Fourier transform of the proton spin density, weighted by the Fourier anomalies. Since the k-space measurements are subject to the effects of such weighting during data acquisition, these effects can be accounted for separately or simultaneously in the process of Fourier reconstruction.

In order to relate the signal and noise characteristics of k-space measurements to reconstructed voxel measurements, the complex-valued matrix application of the inverse Fourier transformation was described through a real-valued isomorphism by Rowe et al. [17]. Representing the Fourier reconstruction as a single matrix operator formed the basis for the study in [18] where a mathematical framework, AMMUST-k (A Mathematical Model for Understanding the STatistical effects of k-space preprocessing), was developed to represent various spatial processing operations performed on acquired spatial frequencies in terms of real-valued linear isomorphisms. Representing the reconstruction and image processing operations in this way made it possible to directly compute the exact covariance structure, and ultimately correlation induced into the image-space data, which can result in misleading conclusions in fcMRI and fMRI studies [18–20].

In this manuscript, we expand upon the AMMUST-k framework by modifying the real-valued Fourier reconstruction (FR) operator in such a way that it can account for the effects of $T_2{}^*$, ΔB, and T_1 on the image-space data. As noted before, the measured "actual" k-space data are scaled according to time that has elapsed since the RF excitation pulse and the factors determined by the terms include $T_2{}^*$, ΔB, and T_1. As such, we first develop a real-valued Fourier encoding (FE) operator that considers such weighting, then, we create the modified FR operator by inverting the modified FE operator to account for the encoding effects in image space. The use of a modified FR operator within this framework makes it possible to more accurately reconstruct the image space voxel values from measured spatial frequencies, and also precisely quantify the statistical effects of such correction on the reconstructed data.

The linear Fourier reconstruction operators are first developed by considering different combinations of the Fourier anomalies and examples of each anomaly are shown on a small 8×8 data set. The Fourier operators are then used to theoretically examine the image space data associated with the effects of the Fourier anomalies on a 96×96 digital phantom. The exact mean and induced correlations modified by the adjusted FR operators on both complex-valued and magnitude-squared data are also illustrated by using the proposed model. The results of the proposed FE anomaly correction framework are also illustrated on acquired experimental human subject fMRI data by focusing on the incorporation of the longitudinal relaxation time, T_1. Finally, a comparison is made between the activation statistics computed from the reconstructed data with and without the incorporation of T_1 effects with the use of both conventional magnitude-only [21] and newer complex-valued fMRI activation models [22–25].

2. Theory

2.1. Complex-valued image reconstruction in fMRI

In fMRI, complex-valued measurements are acquired discretely in time corresponding to two-dimensional spatial frequency measurements. The measurements are then reconstructed into a complex-valued image by applying the complex-valued inverse Fourier transformation. Although the original object, proton spin density, is real-valued, imperfections in the imaging process lead to a complex-valued image.

When the complex-valued Fourier reconstruction is described through a real-valued isomorphism [17], a vector of the reconstructed image, y, can be written as the product of a FR operator, Ω, with a vector of the observed k-space observation, s, by

$$y = \Omega s. \tag{1}$$

Similarly, the vector of the k-space observation, s, can be written as the product of a FE operator, $\overline{\Omega} = \Omega^{-1}$, with a vector of the reconstructed image, y, as

$$s = \overline{\Omega} y. \tag{2}$$

In Eqs. (1) and (2), $y=(y_R{}',y_I{}')'$ is a $2p\times 1$ vector with the real parts of p image values, $y_R=(y_{R1},\ldots,y_{Rp})'$, stacked above the imaginary parts of p image values, $y_I=(y_{I1},\ldots,y_{Ip})'$, for an $m\times n$ image of $p = mn$ voxels. Similarly, $s=(s_R{}',s_I{}')'$ is a $2p\times 1$ vector with p real parts, $s_R=(s_{R1},\ldots,s_{Rp})'$, stacked above p imaginary parts, $s_I=(s_{I1},\ldots,s_{Ip})'$, for a Cartesian acquisition of k-space. Thus, the FR and FE operators, Ω and $\overline{\Omega}$, have dimensions of $2p\times 2p$. The Cartesian FR operator can be represented as

$$\Omega = \begin{pmatrix} \mathrm{Re}(\Omega_C) & -\mathrm{Im}(\Omega_C) \\ \mathrm{Im}(\Omega_C) & \mathrm{Re}(\Omega_C) \end{pmatrix}, \tag{3}$$

where $\mathrm{Re}(\cdot)$ and $\mathrm{Im}(\cdot)$ denote the real and imaginary parts of their respective arguments. The matrix Ω_C is defined as the Kronecker product of the matrices, Ω_x and Ω_y, as $\Omega_C=\Omega_x\otimes\Omega_y$, where the matrices Ω_x and Ω_y Fourier transform the columns and the rows of the acquired k-space measurements, respectively. The jk^{th} element of the FR operator Ω_x can be written as $(\Omega_x)_{jk} = w^{((-n/2)+(j-1))((-n/2)+(k-1))}$, where j and k are the indices from 1 to n and $w=(1/n)\exp(i2\pi/n)$. The matrix Ω_y follows similarly with n replaced by m. The Fourier encoding operator, $\overline{\Omega}$, has a similar skew symmetric form to Ω where $w=\exp(-i2\pi/n)$. The operators, Ω and $\overline{\Omega}$, will be considered as the standard FR and FE operators as they do not account for any Fourier anomalies.

As the real-valued spatial frequency vector, s, contains complex-values, the application of the FR operator in Eq. (1) produces a covariance between the real measurements, between the imaginary

measurements, and between the real and imaginary measurements. If the k-space vector, s, has a covariance matrix, Γ, then the covariance matrix of the reconstructed image, y, becomes

$$\mathrm{cov}(y) = \Omega\Gamma\Omega', \tag{4}$$

where the operator "′" denotes the transpose of a matrix.

To produce the required k-space vector, s, the acquired k-space array, which is observed as a pairing of real and imaginary component of each frequency can be reordered by reversing the alternating rows of measurements and segregating real and imaginary observations through permutation matrices, P_A and P_S. Since the k-space data include extra points acquired during the phase encoding blips in echo planar imaging, the acquired measurements also need to be censored by the censoring matrix, P_E. Additionally, Nyquist ghosting can be corrected through a series of linear operators that reorders to group the real and imaginary observations from each line together (P_R), Fourier transform each row (Ω_R), shift the phase of the each transformed row (Φ_N), and finally apply the inverses of Ω_R and P_R. These k-space operators together with additional operators that can include Fourier homodyne interpolation, H, zero-filling, F, apodization, A, and explicit image space smoothing operator, S, can be combined into a single operator, O, that signifies the series of all linear operators applied to s [18]. Therefore, the reconstruction in Eq. (1) simplifies to

$$y = Os, \tag{5}$$

where O represents a multiplication of operators applied throughout the image reconstruction process,

$$O = S\Omega AFHP_R{}^{-1}\Omega_R{}^{-1}\Phi_N\Omega_R P_R P_S P_A P_E. \tag{6}$$

If $\mathrm{E}(s) = s_0$ and $\Gamma = \mathrm{cov}(s)$, then mean and covariance of the reconstructed image vector, y, are altered by the final operator, O, to become

$$E(y) = Os_0$$

and

$$\mathrm{cov}(y) = O\Gamma O'. \tag{7}$$

The correlation structure between voxels in y can be calculated from $cov(y)$ by

$$corr(y) = D^{-1/2}O\Gamma O'D^{-1/2}, \tag{8}$$

where D is a diagonal matrix of the variances drawn from the diagonal of the covariance matrix, $O\Gamma O'$, and the $-1/2$ superscript denotes that the diagonal elements are inverted after taking the square root. The covariance matrices of both the spatial frequencies and the reconstructed image-space values include the following covariance pairs: real by real, imaginary by imaginary, and real by imaginary components of s and y, respectively.

An assumption of normality allows the derivation of the covariance of the square of the magnitude data from the covariance matrix, $cov(y) = O\Gamma O'$ [17,18]. Both magnitude-squared and complex-valued data can be used to analyze changes made to the acquired correlation structures as the correlation of magnitude-squared data is asymptotically equivalent to the magnitude-only correlation and linear in nature.

2.2. Acquired k-space signal and Fourier anomalies

Under the assumption that the complex-valued matrix of two dimensional spatial frequencies is measured instantaneously at the echo time, TE, the acquired k-space signal in an EPI sequence can be expressed through the MR signal equation,

$$s\left(k_x,k_y\right) = \int_{-\infty}^{\infty}\int_{-\infty}^{\infty} M_0(x,y)\left(1-e^{-TR/T_1(x,y)}\right)e^{-TE/T_2{}^*(x,y)}e^{i\gamma\Delta B(x,y)TE}e^{-i2\pi\left(k_x x+k_y y\right)}dxdy, \tag{9}$$

where TR is the repetition time and $M_0(x,y)$ is the proton spin density.

Since the signal for different points in k-space is measured at different times, the k-space observation process occurs over a finite duration of time and the signal equation in Eq. (9) can be more accurately expressed as

$$s\left(k_x,k_y\right) = \int_{-\infty}^{\infty}\int_{-\infty}^{\infty} M_0(x,y)\left(1-e^{-TR/T_1(x,y)}\right)e^{-t/T_2{}^*(x,y)}e^{i\gamma\Delta B(x,y)t}e^{-i2\pi\left(k_x x+k_y y\right)}dxdy, \tag{10}$$

where the k-space point (k_x,k_y) is sampled at time $t=t(k_x,k_y)$. As the variable $t=t(k_x,k_y)$ varies for each k-space measurement, both $T_2{}^*$ and ΔB break the Hermitian symmetry of the k-space observations, and could therefore cause artifacts and distortions in the reconstructed images. Moreover, the longitudinal relaxation time, T_1, causes changes in signal intensity depending on the tissue characteristics.

In conventional studies, the term $(1-\exp(-\mathrm{TR}/T_1))$ in Eq. (10) is assumed to be approximately 1, by choosing TR to be much greater than T_1. This reduces Eq. (10) to depend only on $T_2{}^*$ by

$$s\left(k_x,k_y\right) = \int_{-\infty}^{\infty}\int_{-\infty}^{\infty} M_0(x,y)e^{-t/T_2{}^*(x,y)}e^{i\gamma\Delta B(x,y)t}e^{-i2\pi\left(k_x x+k_y y\right)}dxdy, \tag{11}$$

and thus leads to $T_2{}^*$-weighted images.

The assumption of an infinite TR however can never be reached directly since the goal is to image the brain as quickly as possible, thus fast acquisitions are needed. The neglected term, $(1-\exp(-\mathrm{TR}/T_1))$, therefore takes non-negligible values with the parameter settings that are commonly used in fMRI experiments. Presented in Table 1 are the values that $(1-\exp(-\mathrm{TR}/T_1))$ outputs when the relaxation parameter values of gray matter and white matter tissues are measured at 3.0 T [26] and two commonly used TR values, 1000 ms and 2000 ms, are used. It is of note here that the value of $(1-\exp(-\mathrm{TR}/T_1))$ is expected to be slightly lower at 7.0 T which has been widely used in high-field fMRI for study of the human brain. Furthermore, the variations in the value of TR have an essential effect on the control of image contrast characteristics. As such, accounting for T_1 effects has the potential of retaining the image contrast over the time series that exists prior to T_1 equilibrium. The regular FR operator, Ω, is thus modified with the aim of analyzing and accounting for the effects of Fourier anomalies: $T_2{}^*$, ΔB, and T_1.

2.3. Incorporating MR relaxivities to Fourier reconstruction process

In this section, we develop a modified Fourier image reconstruction operator that produces the "ideal" image space vector, y_{Id}, from the "actual" measured k-space vector, s_{Act}, that is affected by the exponential terms for $T_2{}^*$, ΔB, and T_1 during the Fourier encoding process. Consider that the "ideal" image space vector, y_{Id}, would be

Table 1
T_1 exponential term values at 3.0 T.

$1-\exp(-\mathrm{TR}/T_1(x,y))$	TR = 1000 ms	TR = 2000 ms
GM (T_1 = 1331 ms)	0.5283	0.7750
WM (T_1 = 832 ms)	0.6994	0.9096

constructed from the "ideal" k-space vector, s_{Id}, that is not affected by FE anomalies and the "actual" measured signal, s_{Act}, that we acquire in practice is scaled according to a weighting determined by FE anomalies.

As each k-space measurement is approximately expressed as the forward Fourier transform of the spin density, weighted by the MR relaxivities and the magnetic field inhomogeneities at a single point in k-space, we can first incorporate the exponential terms for ${T_2}^*$, T_1, and ΔB into the FE operator, $\overline{\Omega}$. Then, we construct the modified FR operator by taking the inverse of the modified FE operator matrix.

As with the Cartesian Fourier reconstruction operator given in Eq. (3), the Cartesian FE operator is expressed as

$$\overline{\Omega} = \begin{pmatrix} \mathrm{Re}(\overline{\Omega}_C) & -\mathrm{Im}(\overline{\Omega}_C) \\ \mathrm{Im}(\overline{\Omega}_C) & \mathrm{Re}(\overline{\Omega}_C) \end{pmatrix}, \tag{12}$$

where $\overline{\Omega}_C$ is defined as $\overline{\Omega}_C = \overline{\Omega}_x \otimes \overline{\Omega}_y$, and the jk^{th} element of $\overline{\Omega}_x$ can be written as $(\overline{\Omega}_x)_{jk} = w^{((-n/2)+(j-1))((-n/2)+(k-1))}$, where j and k are the indices from 1 to n when $w = \exp(-i2\pi/n)$.

Regardless of the relaxation times or ΔB that causes the weighting difference, in the general case, we can describe the weighting of the MR signal at each point with a two-dimensional array, W, as

$$W\left(k_x, k_y, x, y\right) = \left(1 - e^{-TR/T_1(x,y)}\right) e^{-t\left(k_x,k_y\right)/{T_2}^*(x,y)} e^{i\gamma\Delta B(x,y)t\left(k_x,k_y\right)}. \tag{13}$$

Two dimensional FE anomaly weighting function, W, can be constructed as

$$W\left(k_x, k_y, x, y\right) = \begin{bmatrix} W(1,1,1,1) & \cdots & W(m,n,1,1) \\ \vdots & \ddots & \vdots \\ W(1,1,m,n) & \cdots & W(m,n,m,n) \end{bmatrix},$$

for an $m \times n$ image.

In order to achieve the ideal image space vector, y_{Id}, after reconstruction, we first modify $\overline{\Omega}$ in Eq. (12), by including W into the real-valued isomorphism. The modified FE operator, $\overline{\Omega}_a$, can be created by first performing an element-wise multiplication of the Kronecker product, $\overline{\Omega}_a$, by the FE anomaly weighting function as

$$\overline{\Omega}_{C,a} = \left(\overline{\Omega}_x \otimes \overline{\Omega}_y\right) \circ W\left(k_x, k_y, x, y\right), \tag{14}$$

where $\circ$ represents an element-wise Hadamard product. Finally, the modified FE operator, $\overline{\Omega}_a$, can be expressed as

$$\overline{\Omega}_a = \begin{pmatrix} \mathrm{Re}\left(\overline{\Omega}_{C,a}\right) & -\mathrm{Im}\left(\overline{\Omega}_{C,a}\right) \\ \mathrm{Im}\left(\overline{\Omega}_{C,a}\right) & \mathrm{Re}\left(\overline{\Omega}_{C,a}\right) \end{pmatrix}. \tag{15}$$

The modified FR operator, Ω_a, can then be calculated by $\Omega_a = {\overline{\Omega}_a}^{-1}$.

With the modified FR operator that accounts for the effects of the FE anomalies, the operator, O, in Eq. (6) can be updated to

$$O_a = S\Omega_a AFHP_R{}^{-1}\Omega_R{}^{-1}\Phi_N\Omega_R P_R P_S P_A P_E. \tag{16}$$

The complete process given in Eq. (5) can be written in such a way that the operator, O_a, reconstructs the "actual" measured k-space vector, s_{Act}, into the "ideal" corrected image space vector, y_{Id}, as

$$y_{Id} = O_a s_{Act}. \tag{17}$$

The inclusion of ${T_2}^*$, ΔB, and T_1 finely alters the structure of the standard FE and FR operators, $\overline{\Omega}$ and Ω to arrive at $\overline{\Omega}_a$ and Ω_a. The alterations caused by the FE anomalies in the FE operator, and in the FR operator that accounts for such alterations can be better seen in a low-dimensional example than a real size data set. Presented for an 8×8 example, the 128×128 arrays in Fig. 1(a) and (c) are the FE and FR operators that either do not account for any terms (standard operators), or separately account for the ${T_2}^*$ decay, ΔB in the frequency encoding direction, and the T_1 recovery term. T_2^* and T_1 maps were considered in the example map which were scaled to values from 80 to 100 ms and 800 to 1000 ms inside the phantom, respectively. The ΔB term was modeled as a linear gradient ranging from 0 to 2.5×10^{-6} T. It can be seen in the second and third panels of Fig. 1(a) and (c) that the incorporation of ${T_2}^*$ and T_1 recovery causes amplitude change in the modified FE and FR operators for the considered TR and TE values. One can observe that the modified FE operator that includes ${T_2}^*$ and T_1, given in the second and third panels of Fig. 1(a), is visually different from the standard FE operator. Since $\exp(-t/T_2^*)$ in Eq. (13) converges to 0 for the voxels that have small ${T_2}^*$ values, the element values of the modified FE operator in the second panel tend toward zero in the portions that correspond to these voxels with low T_2^* value. Moreover, the operators that incorporate ΔB effects that are given in the fourth panel of Fig. 1(a) and (c) appear to be clearly different than the standard arrays as a result of the linear gradient change in magnetic field.

For a better illustration of the effects of the anomalies on the FE and FR operators, the difference maps of the standard FE and FR operators with their modified versions that separately account for the effects of ${T_2}^*$, T_1, and ΔB are given in Fig. 1(b) and (d), respectively. It can be observed from the first and second panels of Fig. 1(b) and (d) that the most noticeable difference occurs from the ${T_2}^*$ and T_1 weighting of the voxels that have low T_2^* and high T_1 values. This appears as horizontal and vertical bands in the difference maps of the FE and FR operators, respectively. The third panel of Fig. 1(b) shows that the linear gradient changes in magnetic field cause changes in every element of the standard FE operator as its effect is not voxel-dependent. A similar modification can also be observed in the FR operator that accounts for the ΔB effect given in the third panel of Fig. 1(d).

3. Methods

3.1. Theoretical illustration

To theoretically illustrate the performances of the developed Fourier reconstruction operators, a single-slice of data was generated from a noiseless digital brain phantom. In order to replicate the process of acquiring data from an MRI scanner with a standard EPI pulse sequence, a single time point complex-valued spatial frequency data, $s(k_x,k_y)$, was generated using the MR signal equation given in Eq. (10) under various cases in which T_2^*, T_1, and/or ΔB is considered. Simulated at 3 T, the proton spin density, M_0, in a 96×96 phantom in Fig. 2(a) was used with model ${T_2}^*$ and T_1 values that vary from 42 to 2200 ms for ${T_2}^*$, and from 832 to 4000 ms for T_1, as given in Fig. 2(b) and (c) [26]. The ΔB was considered as a left to right gradient from 0 to 2.5×10^{-6} T, as shown in Fig. 2(d). The timing of the k-space sampling scheme was as in a standard EPI pulse sequence for a 96×96 acquisition matrix, with a bandwidth of 250 kHz, an effective echo spacing of 0.72 ms, an echo time of 50 ms, and a TR of 1 s. The phase encoding direction was assumed to be oriented as posterior to anterior (bottom to top in images).

In our calculations for the theoretical illustration, we consider the k-space operators: P_E, P_A, P_S, P_R, Ω_R, Φ_N, ${\Omega_R}^{-1}$, ${P_R}^{-1}$ and the FR operator, Ω or $\overline{\Omega}_a$, depending on our analysis. Thus, the altered mean and the induced covariance matrix by the applied operators can be calculated according to Eq. (7) by

$$E(y_{Id}) = \Omega_a P_R^{-1}\Omega_R^{-1}\Phi_N\Omega_R P_R P_S P_A P_E s_{Act}$$

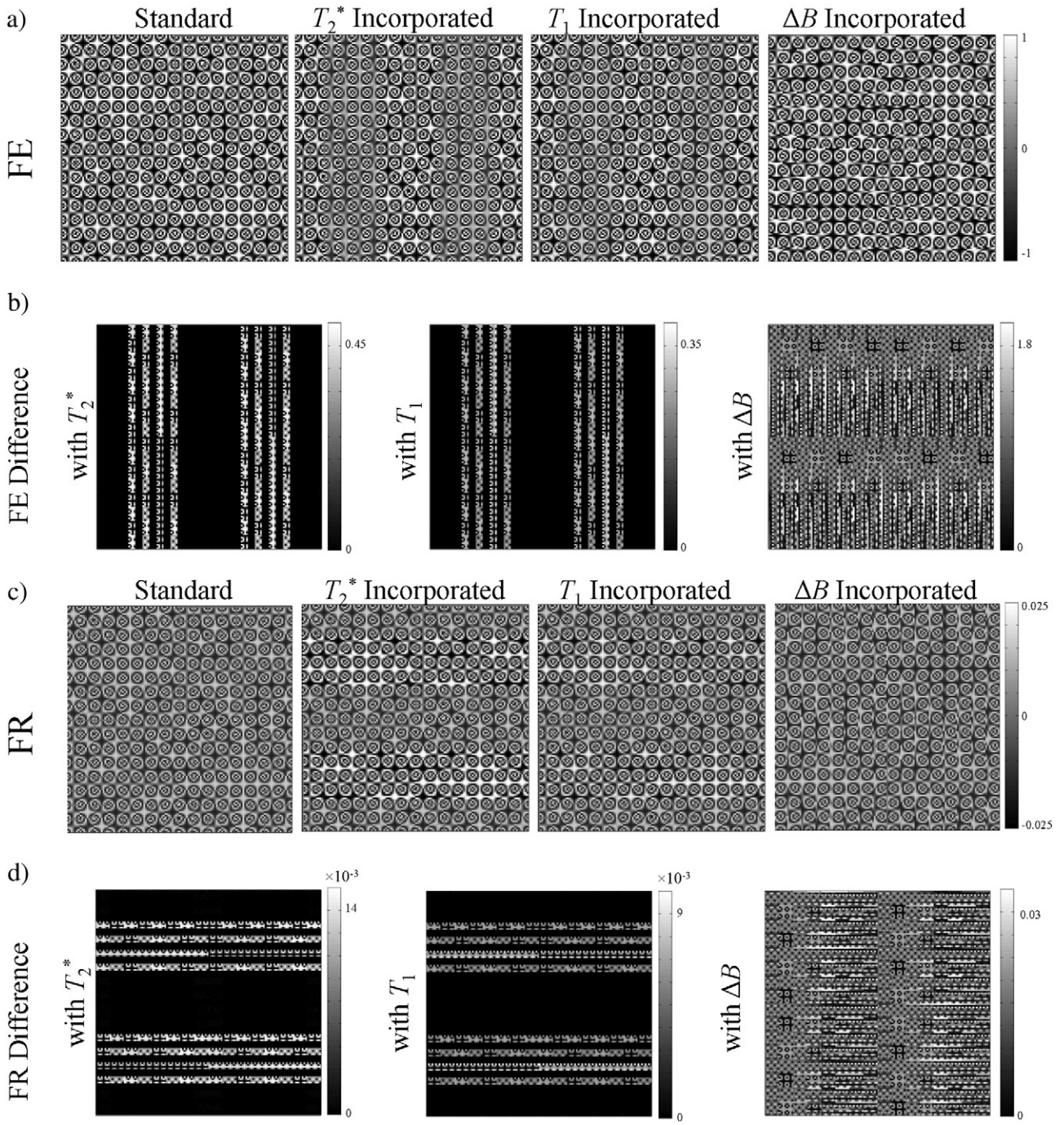

Fig. 1. a) and c) Standard FE and FR operators, $\overline{\Omega}$ and Ω, in the first panel; modified FE and FR operators, $\overline{\Omega}_a$ and Ω_a, that separately account for the effects of T_2^*, T_1, or ΔB in the second, third, and fourth panels, respectively. Absolute difference maps between $\overline{\Omega}$ and $\overline{\Omega}_a$ and between Ω and Ω_a are given in b) and d) for the cases of T_2^*, T_1, or ΔB incorporation in the first, second, and third panels, respectively.

and

$$\mathrm{cov}(y_{ld}) = \left(\Omega_a P_R^{-1} \Omega_R^{-1} \Phi_N \Omega_R P_R P_S P_A P_E\right) \Gamma \left(P_E{}' P_A{}' P_S{}' P_R{}' \Omega_R{}' \Phi_N{}' \left(\Omega_R^{-1}\right)' \left(P_R^{-1}\right)' \Omega_a{}'\right). \tag{18}$$

It should be noted that if $\Gamma = I$, then Eq. (18) reduces to

$$\mathrm{cov}(y_{ld}) = \Omega_a \Omega_a{}', \tag{19}$$

since when each of the operators, except Ω_a, in Eq. (18) is multiplied by their transposes, the products yield identity matrices. Therefore, the altered covariance and correlations will only result from the use of the modified FR operator, Ω_a.

In order to examine the effects of FE anomalies on the reconstructed image space data, we use the data that are generated by considering the individual and sequential effects of T_2^*, ΔB, and T_1 in the frequency space. Then, we perform the Fourier reconstruction with the use of the standard FR operator, Ω, to visually illustrate the alterations that are caused by the FE anomalies if they are not accounted for. Finally, we perform the Fourier reconstruction with the use of the proposed modified FR operator, Ω_a, on the same data set in order to present the performance of Ω_a in accounting for such

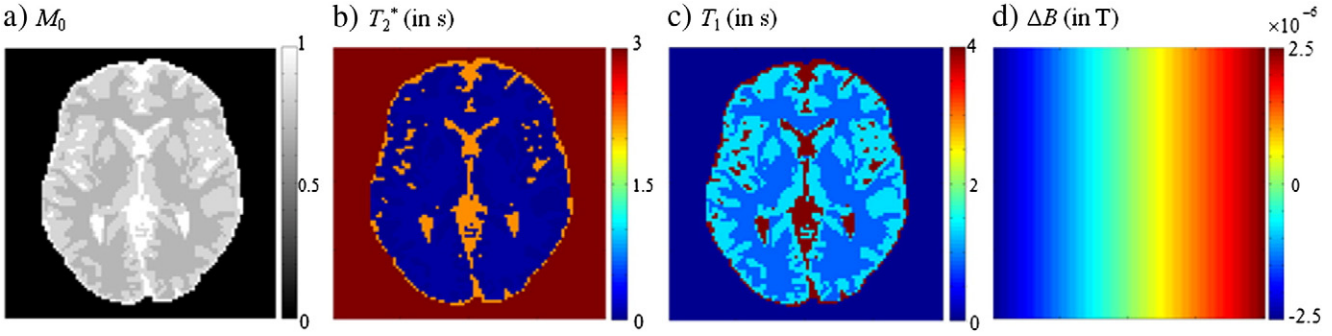

Fig. 2. Parameters considered in theoretical calculations. a) Proton spin density, M_0, (GM:0.83, WM:0.71, CSF:1), b) intra-acquisition decay, T_2^* (GM:0.042 s, WM:0.049 s, CSF:2.2s), c) longitudinal relaxation time, T_1 (GM:1.331 s, WM:0.832 s, CSF:4s), d) B-field inhomogeneity, ΔB (left to right linear gradient changing from 0 to 2.5×10^{-6} T).

effects. Presented in Fig. 3 are the magnitude, phase, real, and imaginary images that are reconstructed from the data sets generated with the effects of T_2^* in Fig. 3(a_1), and (a_2), the effects of ΔB in Fig. 3(b_1), and (b_2), the effects of T_1 in Fig. 3(c_1), and (c_2), and finally the combined effects of T_2^*, ΔB, and T_1 in Fig. 3(d_1), and (d_2). Fig. 3(a_1), (b_1), (c_1), and (d_1) shows the images that are reconstructed with the use of the standard FR operator, Ω, whereas Fig. 3(a_2), (b_2), (c_2), and (d_2) illustrates the images that are reconstructed with the use of the modified FR operator, Ω_a. In this manuscript, we denote the images as "standard-reconstructed" when the standard FR operator is used for reconstruction while we denote images as "modified-reconstructed" when the FR operator, modified to correct the effects of the respective FE anomaly, is used. When generating data for the results presented in Fig. 3, the "true" magnitude of each image is assumed to be the proton spin density as given in Fig. 2(a), and the phase is originally assumed to be zero throughout the image.

The reconstructed image results that are presented in Fig. 3(a_1) and (a_2) are obtained from the frequency space data that are generated by incorporating only the exponential term, $\exp(-t(k_x,k_y)/T_2^*(x,y))$, in such a way that the FE anomaly weighting function, introduced in Eq. (13), is assumed to be $W(k_x,k_y,x,y)=\exp(-t(k_x,k_y)/T_2^*(x,y))$. It can be seen in Fig. 3(a_1) that the magnitude and real images show blurring and loss of image intensity effect that T_2^* causes on the edges of the phantom when the considered T_2^* effect is not corrected. The standard-reconstructed imaginary image shows some artificial imaginary data mostly at the edges of the tissues in the phantom. The modified-reconstructed magnitude, phase, real and imaginary images that are given in Fig. 3(a_2) appear to be exactly the same as the true magnitude, phase, real and imaginary images. This outcome illustrates that Ω_a successfully corrects the T_2^* effect on the reconstructed images.

Fig. 3(b_1) illustrates the standard-reconstructed images whereas Fig. 3(b_2) presents the modified-reconstructed images from the data generated with only B-field inhomogeneity effects. The frequency space data are generated by considering only the exponential term, $\exp(-i\gamma\Delta B(x,y)t(k_x,k_y))$, in such a way that the FE anomaly weighting function in Eq. (13) is assumed to be $W(k_x,k_y,x,y)=\exp(-i\gamma\Delta B(x,y)t(k_x,k_y))$. The B-field inhomogeneity, ΔB, is known to produce image warping and bulk shift in the phase encoding direction in magnitude and real images, as it can be seen in Fig. 3 (b_1). Slight warping can also be observed in the vertical frequency encoding direction because of the higher sampling width. As it can be seen in Fig. 3(b_1), B-field inhomogeneity introduces artificial imaginary data. It can also be observed that the phase, real, and imaginary images are not uniform as a result of the sinusoidal oscillation due to the linear field map. As seen in the case that we examine T_2^* effects, the modified-reconstructed images that are given in Fig. 3(b_1) have been successfully corrected through Ω_a.

Presented in Fig. 3(c_1) and (c_2) the standard- and modified-reconstructed images from the data generated with only T_1 recovery term effects. As explained in previous cases, the frequency data generation is performed by assuming that the FE anomaly weighting function in Eq. (13) is $W(k_x,k_y,x,y)=(1-\exp(-TR/T_1(x,y))$. The standard-reconstructed magnitude and real images in Fig. 3(c_1) exhibit decreased image intensity throughout the phantom. The expected increase in tissue contrast, when the images are modified-reconstructed by the operator, Ω_a, is not observable in this simulation since the assumed proton spin density already has significant contrast information. Similarly with the previous results, the modified-reconstructed images have successfully been corrected compared to a standard reconstruction as it is apparent in Fig. 3(c_1).

Figs. 3(d_1) and (d_2) illustrates the standard- and modified-reconstructed images from frequency space data that are generated with a combination of T_2^*, ΔB, and T_1. The effects of all three terms (blurring, image warping and loss of image intensity) can be observed in the standard-reconstructed images in Fig. 3(d_1) while the modified-reconstructed images in Fig. 3(d_2) are the same as the true maps.

The correction of FE anomalies can be considered as a means of data processing, and thus could potentially induce artificial correlations. Our proposed model allows one not only to account for their effects but also to compute the exact image-space statistics (mean, variance and correlation). As explained in Section 2.1, the correlation matrix produced by Eq. (7) is partitioned into the quadrants that include the correlation between the real components (real/real), between the imaginary components (imaginary/imaginary), and between the real and imaginary components (real/imaginary) of the reconstructed image. Furthermore, the correlations of the magnitude-squared data (square of the magnitude-only data) can be derived from the computed complex-valued correlation matrix and can be considered in the analysis of the correlation structure induced by FE anomaly correction during image reconstruction. In order to present the computed correlation structure, we choose the voxel located in the center of the image as the seed voxel and show the correlation between the measurements of the center voxel, and those from all other voxels. The center voxel's induced magnitude-squared, real/real, imaginary/imaginary, and real/imaginary correlations by the modified FR operator, which are illustrated in Fig. 4(a) and (b), are produced by superimposing the computed correlation structure of the center voxel on a gray-scale anatomical phantom image. Presented in Fig. 4(a) are the induced correlation maps for the center voxel when T_2^* is incorporated. Since we have found that separately accounting for ΔB and T_1 effects yields the same results, the maps presented in Fig. 4(b) represent the correlation structure induced by ΔB or T_1 incorporation. It can be seen that the process of accounting for FE anomalies induces a very small amount of correlation in the

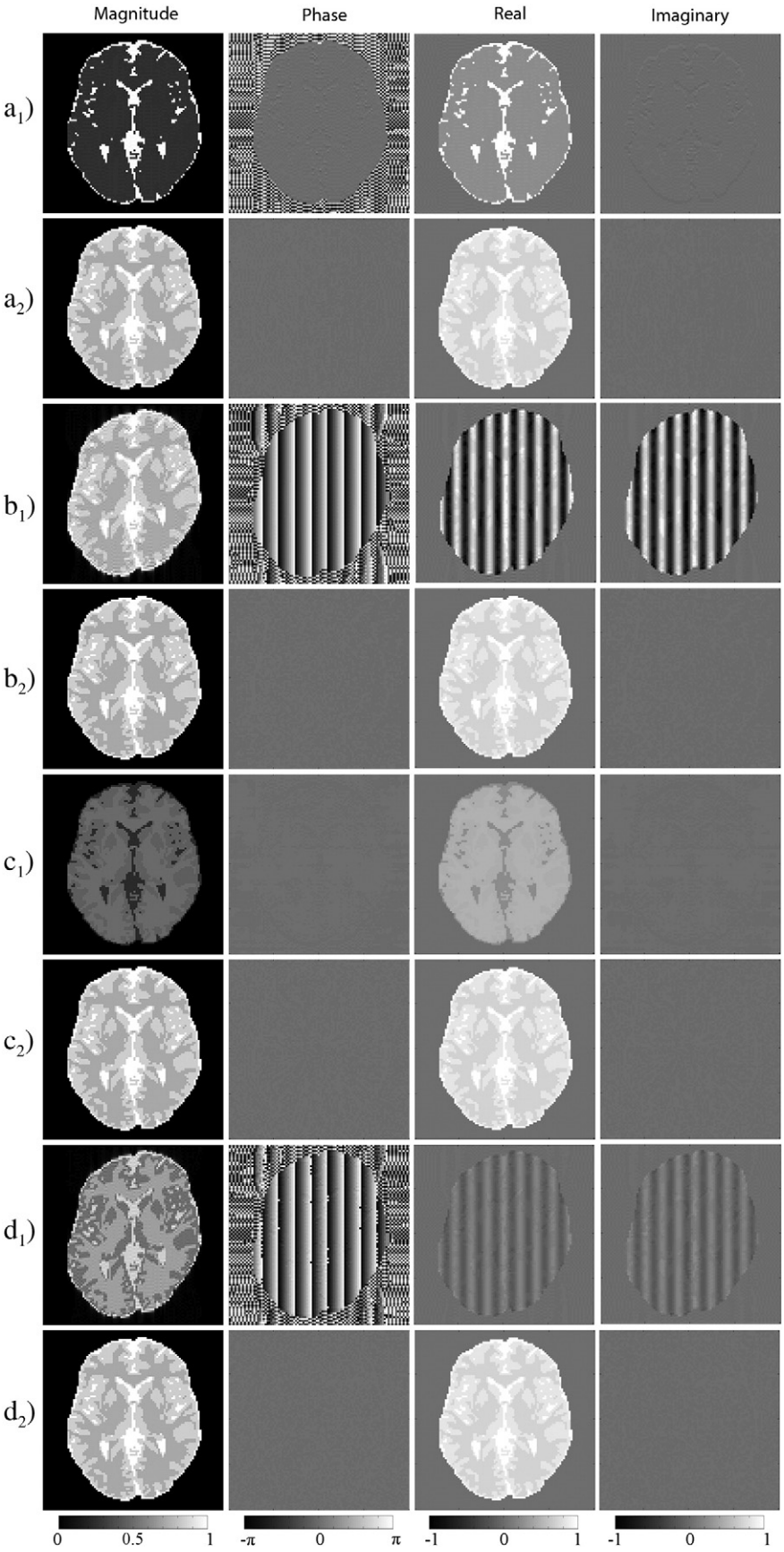

Fig. 3. Reconstructed magnitude, phase, real, and imaginary images from the frequency space data that are generated with the effects of the following FE anomalies: T_2^* in a_1 and a_2, ΔB in b_1 and b_2, T_1 in c_1 and c_2, and T_2^*, ΔB, and T_1 in d_1 and d_2. The images on the rows of a_1, b_1, c_1, and d_1 are standard-reconstructed whereas the images on the rows of a_2, b_2, c_2, and d_2 are modified-reconstructed from the data.

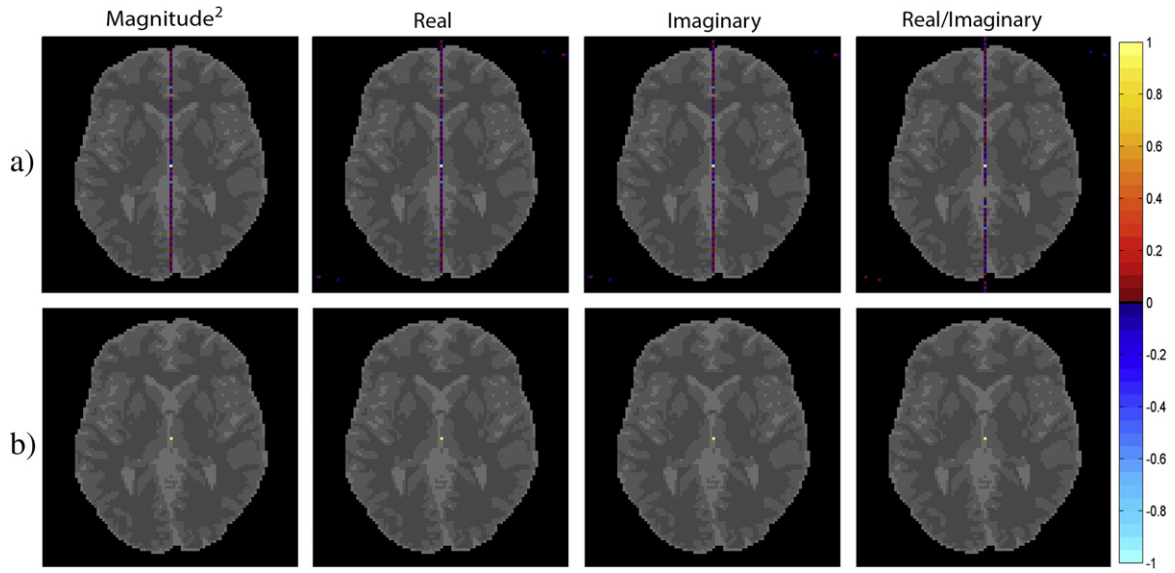

Fig. 4. Presented on a magnitude brain phantom underlay are theoretical image-space magnitude-squared, real/real, imaginary/imaginary, and real/imaginary correlations about the center voxel induced by the modified Fourier reconstruction operator, Ω_a, that accounts for a) T_2^* effects, b) ΔB or T_1 effects. The correlation maps are computed by the linear model, $corr(y) = D^{-1/2}\Omega_a\Gamma\Omega_a{}' D^{-1/2}$, with the assumption of an identity initial spatial covariance, $\Gamma = I$, between voxels.

maps in Fig. 4(a) and no visible correlation in Fig. 4(b). Since little to no correlation is induced, this FE anomaly correction method is ideal for use in experimental human experiments.

3.2. Experimental illustration

A set of human data from a bilateral finger tapping fMRI block design experiment was acquired for a series of 510 time points with a 3.0 T General Electric Signa LX magnetic resonance imager to further illustrate the performance of the proposed modified FR operator. The paradigm followed a block design with an initial 20 s rest followed by 16 epochs of 15 s on and 15 s off. The data set was comprised of seven 2.5 mm thick axial slices that are 96×96 in dimension for a 24.0 cm FOV, with the phase encoding direction oriented as posterior to anterior (bottom to top in images). The data set had an effective echo spacing of 0.72 ms, a flip angle of 90°, and an acquisition bandwidth of 250 kHz. A time varying TE array was constructed to utilize the resulting signal change that allows for the estimation of the relaxation parameters [27]. The echo time was fixed at 42.7 ms for the first 10 and the last 490 time points, i.e. $1 \le t \le 10$ and $21 \le t \le 510$. TE values were then equispaced in the interval of [42.7 ms, 52.7 ms] for $11 \le t \le 15$ and $16 \le t \le 20$.

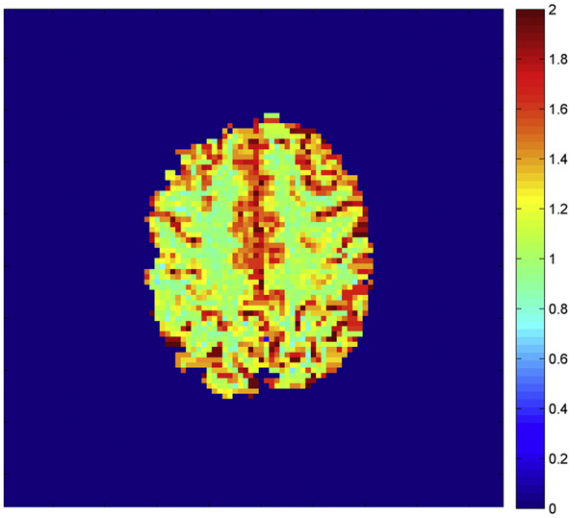

Fig. 5. Estimated T_1 map (in s) from the ratio of the first time course image and the average steady state image. The voxel values outside of the brain region are set to 10^{-6} s.

The application of the proposed linear framework on the acquired data sets is a two-step process, involving the estimation of T_2^*, T_1, and/or ΔB followed by the incorporation of the estimates during the image reconstruction with the use of the modified FR operator. The framework works well when the estimated T_2^*, ΔB, and T_1 maps are close to the actual maps. The use of underestimated or overestimated parameter maps in the proposed framework can potentially cause undesired artifacts in the reconstructed images. For instance, overcorrection of longer T_2^* values results in considerable edge enhancements; and the shorter T_2^* values can suffer from noise amplification [1]. As such, for the experimental illustration of the proposed framework, we focus on incorporation of only T_1 into the FR process since T_1 map can be easily estimated from the measurements acquired during the transient state prior to T_1 equilibrium [28]. However, with accurate estimates of T_2^* and static ΔB maps, the proposed framework can be utilized to incorporate the other Fourier encoding anomalies.

MRI pulse sequences consist of repeated excitation pulses and the magnetization changes in the same way during each repetition. After a number of excitation pulses, the magnetization reaches a steady-state, where the amount of the magnetization at some point in the sequence is the same from one repetition to the next. After reaching the steady-state, the magnetization begins at equilibrium on each repetition. With an assumption of a 90° flip angle, the estimation of T_1 map can be performed from the ratio of the first echo planar imaging time course image and the average steady state image by using a fast T_1 mapping technique introduced in [28]. The steady-state signal for a 90° flip angle is

$$M_{ss} = M_0\left(1 - e^{-TR/T_1}\right)e^{-TE/T_2^*}, \tag{20}$$

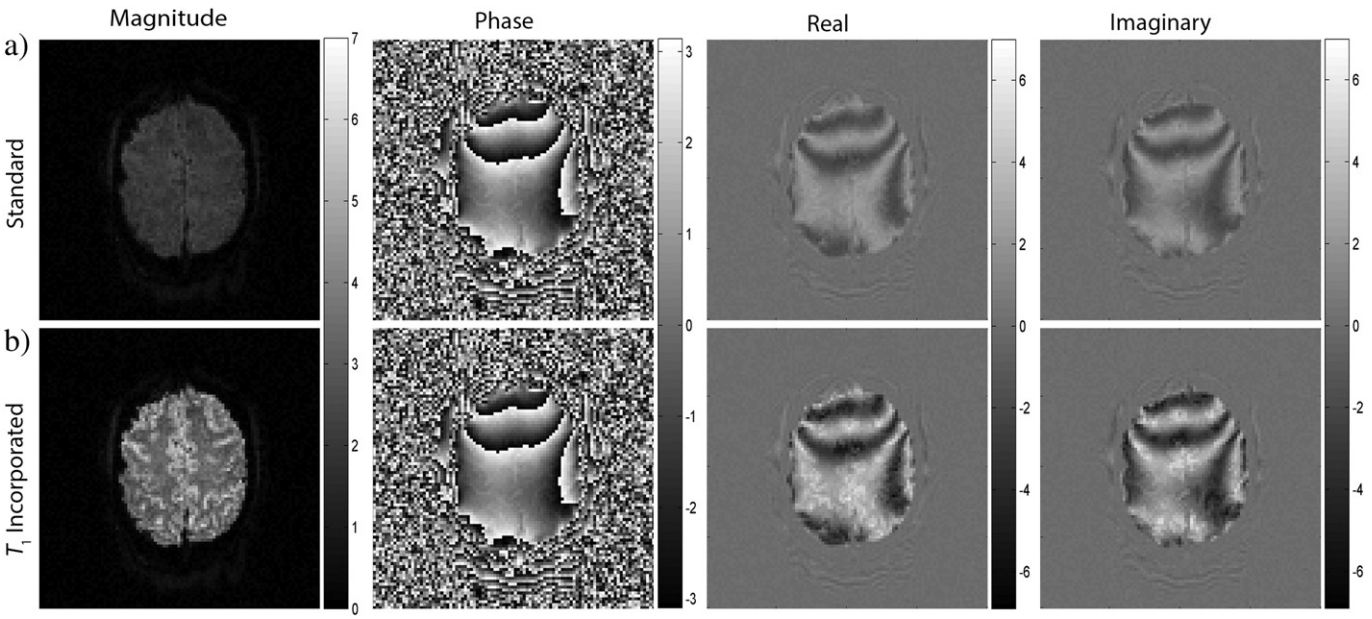

Fig. 6. Reconstructed magnitude, phase, real, and imaginary images at time point $n=21$. a) Images that are reconstructed with the standard FR operator, Ω. b) Images that are reconstructed with the modified FR operator, Ω_a.

whereas the signal for the first echo planar imaging volume is

$$M_1 = M_0 e^{-TE/T_2^*}. \tag{21}$$

By using the ratio of M_1 in Eq. (21) over M_{ss} in Eq. (20), $R = M_1/M_{ss}$, the value of T_1 for one voxel can be calculated by

$$T_1 = \frac{TR}{\ln\left(\frac{R}{R-1}\right)}. \tag{22}$$

For the estimation of T_1 map from the acquired data set that we use in our experimental illustration, the steady state signal, M_{ss}, is computed as the average magnitude images at $6 \le t \le 10$ over five time points for each voxel. The estimated T_1 map that is computed by Eq. (22) is shown in Fig. 5. In order to reduce the errors in the final modified-reconstructed images that could result from the T_1 estimation process, the region outside of the brain is masked out in the presented T_1 map. First, the magnitude images at $21 \le t \le 510$ are averaged over the last 490 points of the time series since the data were acquired with a time varying TE in the first 20 time points. In order to generate the binary two-dimensional brain mask that identifies the outside of the brain, the average magnitude image is used as reference. The voxels whose average magnitude values are larger than the threshold value, which is set as the 26% of the maximum value in the average magnitude image, are given a value of 1 (denoting being in the brain) while the voxels whose values are smaller than or equal to this threshold are set to 10^{-6} (denoting being outside the brain) in the binary mask. The estimated T_1 map is then multiplied by the binary mask image on a voxel-by-voxel basis to mask out the voxels in the region outside the brain.

In order to illustrate the benefits of the incorporation of T_1 into the FR process, we show the magnitude, phase, real and imaginary images that are acquired at the 21st time point, and reconstructed

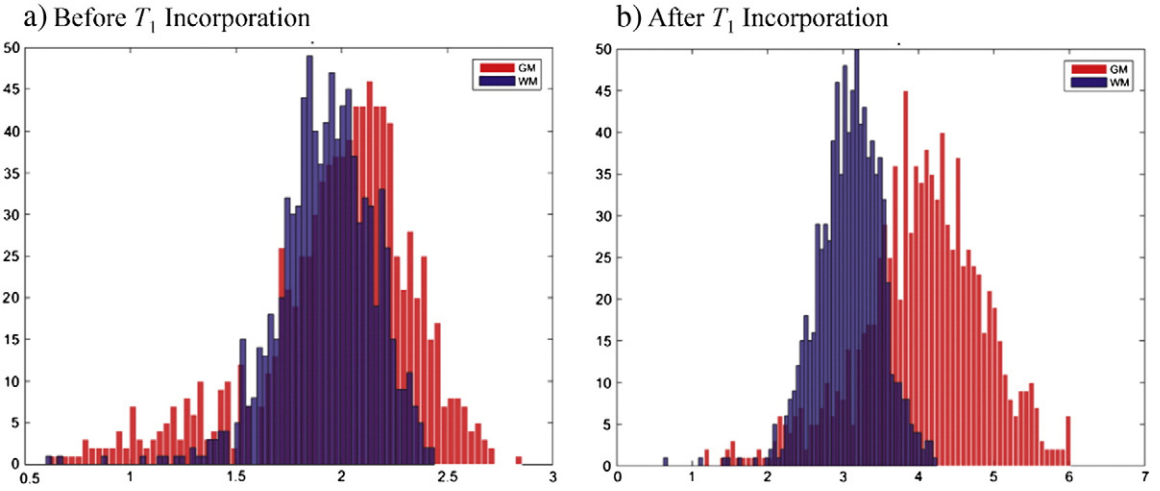

Fig. 7. Histogram plots of the magnitude values from gray matter and white matter voxels that are computed a) before incorporation of T_1 and b) after incorporation of T_1. The plots were generated from the images at time point $n=21$ that were reconstructed with the standard FR operator, Ω, in a) and with the modified FR operator, Ω_a, in b).

Table 2
Signal-to-noise ratios of the whole-brain, gray matter, and white matter areas before and after T_1 incorporation.

	Whole-brain	Gray Matter	White Matter
Before T_1 Incorporation	8.06	8.20	8.00
After T_1 Incorporation	14.76	16.82	12.83

both with the standard FR operator, Ω, and the modified FR operator, Ω_a. Fig. 6(a) shows the standard-reconstructed magnitude, phase, real and imaginary images whereas Fig. 6(b) shows the modified-reconstructed images. It can be observed from Fig. 6 that the incorporation of T_1 leads to an increase in image intensity as well as significantly improved tissue contrast in the magnitude images. Such correction does not alter the phase image while increasing the intensity of the magnitude, real, and imaginary images.

The increase in image contrast provided by T_1 incorporation can be better observed in Fig. 7(a) and (b) in which the histogram plots of the magnitude values from gray matter and white matter voxels that were computed before and after incorporation of T_1 are given, respectively. The plots were generated from the voxel values in the magnitude images in the first panels of Fig. 6(a) and (b). For the segmentation, the estimated T_1 map in Fig. 5 was used, and T_1 ranges were defined predominantly for white matter and gray matter as (0.1 s–1.2 s) and (>1.2 s), respectively. This segmentation resulted in $n_{WM} = 885$ white matter and $n_{GM} = 942$ gray matter voxels. By comparing Fig. 7(a) and (b), one can observe that the contrast between gray matter and white matter regions is significantly improved by the incorporation of T_1 as the white matter and gray matter voxels are more clearly separated in Fig. 7(b) than in Fig. 7(a). This observation is supported by a hypothesis testing analysis for a difference in gray matter and white matter voxel means before and after T_1 incorporation. The test statistic value, t^*, before T_1 incorporation was found to be 3.29 (p-value = 0.0012) whereas it was found to be 31.62 (p-value $< 10^{-10}$) after T_1 incorporation. This strongly implies that the gray–white matter contrast is improved with the use of the proposed method.

The contrast enhancement achieved by the proposed method can also be quantitatively indicated by comparing the gray–white matter contrast-to-noise ratio (CNR) computed before and after T_1 incorporation. The gray–white matter CNRs were separately computed from the magnitude images at time point $n=21$ that were reconstructed with the standard FR operator (given in Fig. 6(a)) and with the modified FR operator that incorporates T_1 (given in Fig. 6(b)). The CNRs were computed from this single image by $CNR_{GM-WM} = |m_{GM} - m_{WM}|/\sigma_O$, where m_{GM} and m_{WM} are the mean magnitude values of the gray matter and white matter areas, and σ_O is the standard deviation of the outside region. A significant increase in CNR_{GM-WM} was observed (before: 0.30 and after: 6.08) with the use of our method for T_1 incorporation.

Furthermore, the application of the proposed method for incorporating T_1 was found to yield an increase in signal-to-noise ratios (SNRs) in whole brain as well as gray and white matter areas as presented in Table 2. The SNR values in Table 2 were computed by $SNR = m_{ROI}/\sigma_O$, where m_{ROI} is the mean magnitude value of the region of interest (whole brain, gray matter or white matter in the table). Our results show that T_1 incorporation increases the SNR by 83%, 105%, and 60% in whole brain, gray matter, and white matter areas, respectively for the single image that was chosen for the analysis.

In order to analyze the possible effects of such correction on the functional activations computed from T_1 incorporated reconstructed images, we show the activation statistics of both standard-reconstructed and modified-reconstructed images in Fig. 8(a), (c) and (b), (d), respectively. Fig. 8(a) and (b) shows the activation t-statistics computed by using the likelihood ratio tests from the MO Model [21]. Illustrated in Fig. 8(c) and (d) are the activation Z-statistics computed by using the CV Model [22–25]. The activation maps shown in Fig. 8 were thresholded at a 5% per comparison error rate [29] and presented with a color bar that ranges between −6.5 and 6.5. It can be observed that the activation statistics that are computed from the standard-reconstructed and the modified-reconstructed image space measurements are identical for both the CV and MO Models. It can be concluded that T_1 incorporation into the Fourier image reconstruction process preserves the functional activations. This result is expected since the estimated T_1 map that is incorporated during the image reconstruction is constant over the time series and therefore the activation information is preserved with the proposed framework.

4. Conclusion

The model developed in this work is based upon the mathematical linear framework for Fourier image reconstruction in a real-valued isomorphism presented in [17] and expanded to the AMMUST-k framework in order to include frequency space processing operations in [18]. We further expand this framework to account for the effects of relaxation parameters, T_2^* and T_1, and magnetic field inhomogeneities, ΔB, that alter the observed MR signal in the process of Fourier encoding. We develop a modified FR operator that accounts for such effects in image space by first generating the modified FE operator that considers the terms of these anomalies as they appear in the signal equation, and then inverting. Although the effects of T_2^* and ΔB have been aimed to be corrected prior to the final analysis of fMRI data in previous studies, the T_1 recovery term has been ignored with the assumption of long repetition time, which is not always met, especially when performing fast repetitive excitations. Furthermore, the T_1 estimates have the potential to detect tissue characteristics of the acquired MRI data.

We present theoretical results for accounting for the effects of T_2^*, ΔB, and T_1 during the Fourier reconstruction process, and focus on incorporating T_1 in acquired echo planar data. The experimental

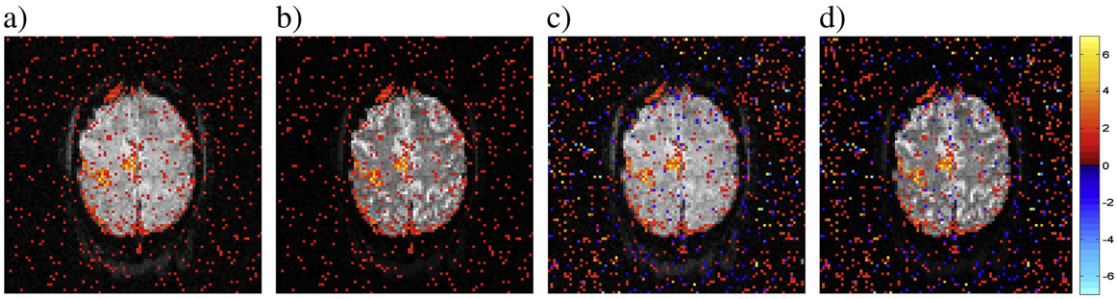

Fig. 8. Activation statistics that are computed from a) standard-reconstructed images with the use of the MO Model, b) modified-reconstructed with the use of the MO Model, c) standard-reconstructed images with the use of the CV Model, d) modified-reconstructed with the use of the CV Model. The activation maps are thresholded at a 5% per comparison error rate.

results presented in this manuscript have shown that the images reconstructed through the use of the reconstruction operator adjusted for estimated static T_1 appear to be brighter and have increased tissue contrast. The method presented in this work can provide improved tissue segmentation over the course of time series, and as suggested in prior studies [13–16], this increased gray/white matter contrast can improve the precision of motion correction and image registration. Furthermore, our experimental results show that such correction does not alter the activation results in an EPI based BOLD fMRI experiment. Even though we incorporate only T_1 into the reconstruction process in experimental analysis, the model can be utilized to account for T_2^* and ΔB effects once their estimated maps are obtained.

The proposed framework makes it possible to precisely quantify any potential induced correlations by the process of accounting for FE anomalies. It has been shown that ΔB and T_1 incorporation does not induce any image space correlations whereas accounting for T_2^* effect induces negligible correlation in the phase encoding direction. The FA correction methods introduced in this manuscript can be used on a regular basis in every fMRI and fcMRI experiment.

As noted before, the proposed method requires an additional step of estimating T_1, T_2^*, and/or ΔB before performing the incorporation of the anomalies into the reconstruction process. Variations in the RF transmit field can cause non-uniform B_1 field strengths creating flip angle variations over the field of view that can lead to non-uniformities across the MRI image and thus errors in image-based quantitative measurements, including T_1 estimation. Inaccuracy of the estimated T_1 map as a result of non-uniformity in B_1 field, especially at high field strength, could potentially reduce the benefit of the proposed method as the T_1 incorporated reconstructed images could be inaccurate. One possible solution to this problem is to produce an accurate map of the non-uniform B_1 field map and correct the intensity inhomogeneities that arise from B_1 non-uniformity [30–33] before performing T_1 estimation.

Recovering image contrast in EPI acquisitions by incorporating T_1 with the use of the proposed framework can be specifically useful for 3D EPI fMRI acquisitions which provide higher temporal SNR and stronger statistical power in activation detection. As 3D EPI yields increased T_1 contrast between tissue types due to the short TR and thus more accurate T_1 estimation, the benefits of our proposed method can be significantly observed in 3D EPI experiments. The method provides higher signal characteristics, such as increased SNR and gray–white matter CNR, more detailed structural information in the reconstructed images, and ultimately reduction in the registration errors in one step from a single pulse sequence as it does not require the acquisition of the anatomical T_1-weighted data.

Acknowledgements

This work was supported by NIH NS087450. The digital phantom that is used to present theoretical illustration results in this manuscript was provided by Volkan Emre Akpinar from the Department of Neurosurgery at Medical College of Wisconsin in Milwaukee, WI.

References

[1] Stroman PW. Essentials of functional MRI. Florida: CRC Press; 2011.
[2] Haacke EM, Brown R, Thompson M, Vankatesan R. Magnetic resonance imaging: physical principles and sequence design. New York: John Wiley and Sons; 1999.
[3] Jezzard P, Balaban RS. Correction for geometric distortion in echo planar images from B0 field variations. Magn Reson Med 1995;34:65–73.
[4] Reber PJ, Wong EC, Buxton RB, Frank LR. Correction of off resonance-related distortion in echo-planar imaging using EPI-based field maps. Magn Reson Med 1998;39:328–30.
[5] Kannengiesser SA, Wang Y, Haacke EM. Geometric distortion correction in gradient-echo imaging by use of dynamic time warping. Magn Reson Med 1999; 42:585–90.
[6] Hahn AD, Rowe DB. Physiologic noise regression, motion regression, and TOAST dynamic field correction in complex-valued fMRI time series. Neuroimage 2012; 59:2231–40.
[7] Hahn AD, Nencka AS, Rowe DB. Enhancing the utility of complex-valued functional magnetic resonance imaging detection of neurobiological processes through postacquisition estimation and correction of dynamic B0 errors and motion. Hum Brain Mapp 2012;33:288–306.
[8] Maclaren JR, Bones PJ, Millane RP, Watts R. MRI with TRELLIS: a novel approach to motion correction. Magn Reson Imaging 2008;26:474–83.
[9] Bernstein MA, King KF, Zhou XJ. Handbook of MRI pulse sequences. Burlington: Elsevier; 2004.
[10] Zhou XJ, Liang Z, Cofer GP, Beaulieu CF, Suddarth SA, Johnson G. Reduction of ringing and blurring artifacts in fast spin-echo imaging. Magn Reson Imaging 1993;3:803–7.
[11] Robitaille P, Berliner L. Ultra high field magnetic resonance imaging. Berlin: Springer; 2007.
[12] Mazaheri Y, Biswal BB, Ward BD, Hyde JS. Measurements of tissue T1 spin lattice relaxation time and discrimination of large draining veins using transient EPI data sets in BOLD-weighted fMRI acquisitions. Neuroimage 2006;32:603–15.
[13] Saad ZS, Glen DR, Chen G, Beauchamp MS, Desai R, Cox RW. A new method for improving functional-to-structural MRI alignment using local Pearson correlation. Neuroimage 2009;44:839–48.
[14] Rowland DJ, Garbow JR, Laforest R, Snyder AZ. Registration of [F-18] FDG microPET and small-animal MRI. Nucl Med Biol 2005;32:567–72.
[15] Vaquero JJ, Desco M, Pascau J, Santos A, Lee I, Seidel J, et al. PET, CT, and MR image registration of the rat brain and skull. IEEE Trans Nucl Sci 2001;48:1440–5.
[16] Gonzalez-Castillo J, Duthie KN, Saad ZS, Chu C, Bandettini PA, Luh W. Effects of image contrast on functional MRI image registration. Neuroimage 2013;67: 163–74.
[17] Rowe DB, Nencka AS, Hoffman RG. Signal and noise of Fourier reconstructed fMRI data. J Neurosci Methods 2007;159:361–9.
[18] Nencka AS, Hahn AD, Rowe DB. A mathematical model for understanding statistical effects of k-space (AMMUST-k) preprocessing on observed voxel measurements in fcMRI and fMRI. J Neurosci Methods 2009;181:268–82.
[19] Bruce IP, Karaman MM, Rowe DB. A statistical examination of the SENSE reconstruction via an isomorphism representation. Magn Reson Imaging 2011; 29:1267–87.
[20] Karaman MM, Nencka AS, Bruce IP, ROWE DB. Quantification of the statistical effects of spatiotemporal processing of non-task fMRI data. Brain Connect 2014;4(9):649–61.
[21] Bandettini PA, Jesmanowicz A, Wong EC, Hyde JS. Processing strategies for time course data sets in functional MRI of the human brain. Magn Reson Med 1993; 30:161–73.
[22] Rowe DB, Logan BR. A complex way to compute fMRI activation. Neuroimage 2004;23:1078–92.
[23] Rowe DB. Parameter estimation in the magnitude-only and complex-valued fMRI data models. Neuroimage 2005;25(4):1124–32.
[24] Rowe DB. Modeling both the magnitude and phase of complex-valued fMRI data. Neuroimage 2005;25:1310-1324.
[25] Rowe DB. Magnitude and phase signal detection in complex-valued fMRI data. Magn Reson Med 2009;62(5):1356–7.
[26] Atlas SW. Magnetic resonance imaging of the brain and spine. Lippincott, PA: Williams & Wilkins; 2008.
[27] Karaman MM, Bruce IP, Rowe DB. A statistical fMRI model for differential T_2^* contrast incorporating T_1 and T_2^* of gray matter. Magn Reson Imaging 2014;32(1):9–27.
[28] Bodurka J, Ye F, Petridou N, Murphy K, Bandettini PA. Mapping the MRI voxel volume in which thermal noise matches physiological noise—implications for fMRI. Neuroimage 2007;34:542–9.
[29] Logan BR, Rowe DB. An evaluation of thresholding techniques in fMRI analysis. Neuroimage 2004;22:95–108.
[30] Mihara H, Iriguchi N, Ueno S. A method of RF inhomogeneity correction in MR imaging. Magn Reson Mater Phys Biol Med 1998;7:115–20.
[31] Trejer R, Steingoetter A, Fried M, Schwizer W, Boesiger P. Optimized and combined T1 and B1 mapping technique for fast and accurate T1 quantification in contrast-enhanced abdominal MRI. Magn Reson Med 2007;57:568–76.
[32] Volz S, Noth U, Rotarsa-Jagiela A, Deichmann R. A fast B_1 mapping method for the correction and normalization of magnetization transfer ratio maps at 3 T. Neuroimage 2010;49:3015–26.
[33] Wang J, Qiu M, Yang QX, Smith MB, Constable RT. Measurement and correction of transmitter and receiver induced non-uniformities in vivo. Magn Reson Med 2015;53:408–17.